ADVANCED MATERIALS
www.advmat.de

Novel Bi-Doped Amorphous SnO_x Nanoshells for Efficient Electrochemical CO_2 Reduction into Formate at Low Overpotentials

*Qi Yang, Qilong Wu, Yang Liu, Shuiping Luo, Xiaotong Wu, Xixia Zhao, Haiyuan Zou, Baihua Long, Wen Chen, Yujia Liao, Lanxi Li, Pei Kang Shen, Lele Duan, and Zewei Quan**

Engineering novel Sn-based bimetallic materials could provide intriguing catalytic properties to boost the electrochemical CO_2 reduction. Herein, the first synthesis of homogeneous $Sn_{1-x}Bi_x$ alloy nanoparticles (x up to 0.20) with native Bi-doped amorphous SnO_x shells for efficient CO_2 reduction is reported. The Bi-SnO_x nanoshells boost the production of formate with high Faradaic efficiencies (>90%) over a wide potential window (−0.67 to −0.92 V vs RHE) with low overpotentials, outperforming current tin oxide catalysts. The state-of-the-art Bi-SnO_x nanoshells derived from $Sn_{0.80}Bi_{0.20}$ alloy nanoparticles exhibit a great partial current density of 74.6 mA cm^{-2} and high Faradaic efficiency of 95.8%. The detailed electrocatalytic analyses and corresponding density functional theory calculations simultaneously reveal that the incorporation of Bi atoms into Sn species facilitates formate production by suppressing the formation of H_2 and CO.

Electrochemical converting greenhouse gas CO_2 into useful renewable fuels is an emerging research area, in which achieving high reaction activity and product selectivity at low overpotential is of vital importance.[1] Compared with the noble metals[2] (Pd, Au, Ag, etc.) and toxic metals[3] (Pb, In, etc.), Sn is an inexpensive, non-toxic and environmentally friendly electrocatalyst for CO_2 reduction. Specially, tin oxides (SnO, SnO_2 and SnO_x) are attractive catalysts for the electrochemical conversion of CO_2 to high-valuable formate, due to their appropriate orbital energy and electronic configuration.[4a] However, the performance of various tin oxides is far from satisfactory, owing to their relatively low intrinsic electrical conductivity and low selectivity toward formate formation at low overpotentials.[4] One alternative strategy for improving catalytic activity and selectivity is to introduce other components (e.g., Ag, Cu, Mn) that have a synergistic effect with Sn to modulate the reactant adsorption, activation and product desorption.[1h,4,5] However, the low formate selectivity (typically <40%) of these catalysts at low overpotentials remains an urgent problem.

To further promote formate production, engineering new Sn-based bimetallic materials has emerged as an efficient strategy. In addition, the high oxygen affinity properties of Sn makes it possible to form core–shell nanostructures with tunable atom-doped tin oxide nanoshells and high electronic conductivity.[6] Another alternative low-cost catalyst of Bi possesses some characteristics that are suitable for CO_2 electrochemical reduction.[1h,7] Recently, several studies reported the unique properties of Sn-Bi eutectic alloys,[8] the orbital interaction effects at the interface between Sn nanosheets and Bi nanoparticles (NPs),[9] and amorphous SnO_x modified by Bi species,[10] which are promising candidates for CO_2 reduction. Nonetheless, the problems of low formate selectivity and high competition with hydrogen evolution at low overpotentials remain unsolved.

Herein, we report the first synthesis of homogeneous $Sn_{1-x}Bi_x$ alloy NPs with remarkably high Bi concentration (x up to 0.20) that naturally form the Bi-doped amorphous SnO_x nanoshells. The state-of-the-art Bi-SnO_x nanoshells derived from $Sn_{0.80}Bi_{0.20}$ alloy NPs exhibit higher selectivities (>90% from −0.67 to −0.92 V, with a maximum value of 95.8% at −0.88 V) and partial current density (74.6 mA cm^{-2}) for the electrochemical reduction of CO_2 to formate than current tin oxide catalysts. Based on experimental results and DFT analyses, the excellent performance of Bi-SnO_x catalysts is revealed to originate from the synergistic effect between incorporated Bi atoms and Sn species, which could facilitate charge-transfer from the electrode to the adsorbed CO_2 and significantly enhance the formate selectivity by suppressing H_2 and CO formation.

Uniform $Sn_{1-x}Bi_x$ alloy NPs were successfully synthesized through the co-reduction of $SnCl_2$ and BiI_3 precursors with tunable molar ratios (refer to Figures S1 and S2 and the Experimental Section in the Supporting Information for details). The typical transmission electron microscopy (TEM)

Q. Yang, Q. Wu, Dr. S. Luo, X. Wu, Dr. X. Zhao, H. Zou, Dr. B. Long, W. Chen, Y. Liao, L. Li, Prof. L. Duan, Prof. Z. Quan
Department of Chemistry, Key Laboratory of Energy Conversion and Storage Technologies, Ministry of Education
Southern University of Science and Technology (SUSTech)
Shenzhen, Guangdong 518055, P. R. China
E-mail: quanzw@sustech.edu.cn
Dr. Y. Liu, Prof. P. K. Shen
Collaborative Innovation Center of Sustainable Energy Materials
Guangxi Key Laboratory of Electrochemical Energy Materials
College of Chemistry and Chemical Engineering
Guangxi University
Nanning, Guangxi 530004, P. R. China
The ORCID identification number(s) for the author(s) of this article can be found under https://doi.org/10.1002/adma.202002822.

DOI: 10.1002/adma.202002822

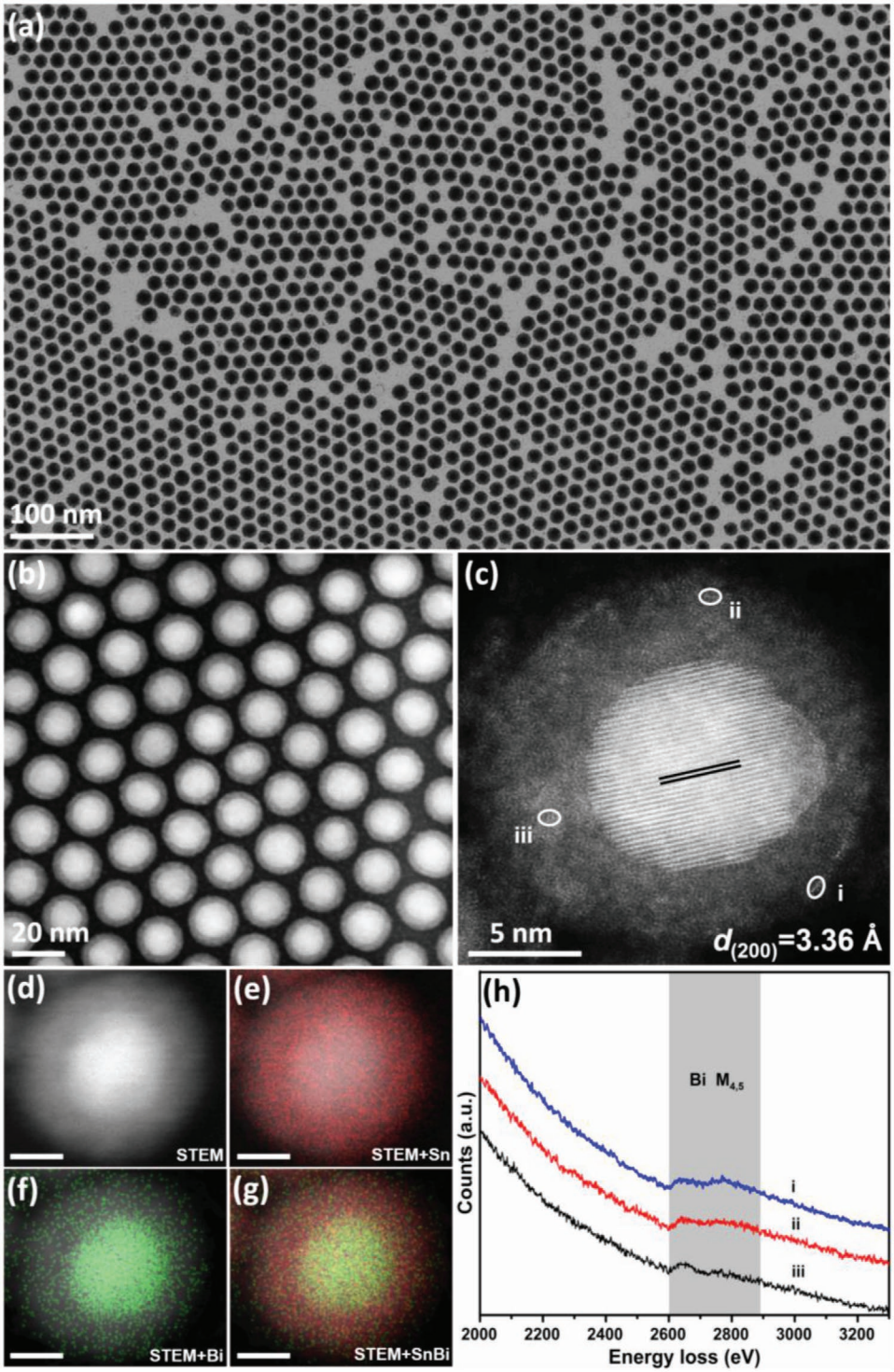

Figure 1. a–c) TEM, HAADF-STEM and aberration-corrected HAADF-STEM images of as-prepared $Sn_{0.80}Bi_{0.20}$ alloy NPs. d–g) EDS elemental mapping images of $Sn_{0.80}Bi_{0.20}$ alloy NPs. h) Corresponding EELS of Bi $M_{4,5}$ acquired at marked points (i–iii) in (c). The scale bars in d–g) represent 5 nm.

and high-angle annular dark-field scanning transmission electron microscopy (HAADF-STEM) images (**Figure 1**a,b) show that $Sn_{0.80}Bi_{0.20}$ alloy NPs are spherical and monodisperse with good size uniformity. Based on the statistics of over 200 NPs, the average size diameter of the $Sn_{0.80}Bi_{0.20}$ alloy NPs is 19.9 ± 1.2 nm, which is similar to those of other $Sn_{1-x}Bi_x$ compositions (Sn, $Sn_{0.93}Bi_{0.07}$, $Sn_{0.86}Bi_{0.14}$), as shown in Figure S3 (Supporting Information). These Sn/Bi atomic ratios were determined by inductively coupled plasma mass spectrometry (ICP-MS). Aberration-corrected HAADF-STEM image (Figure 1c)

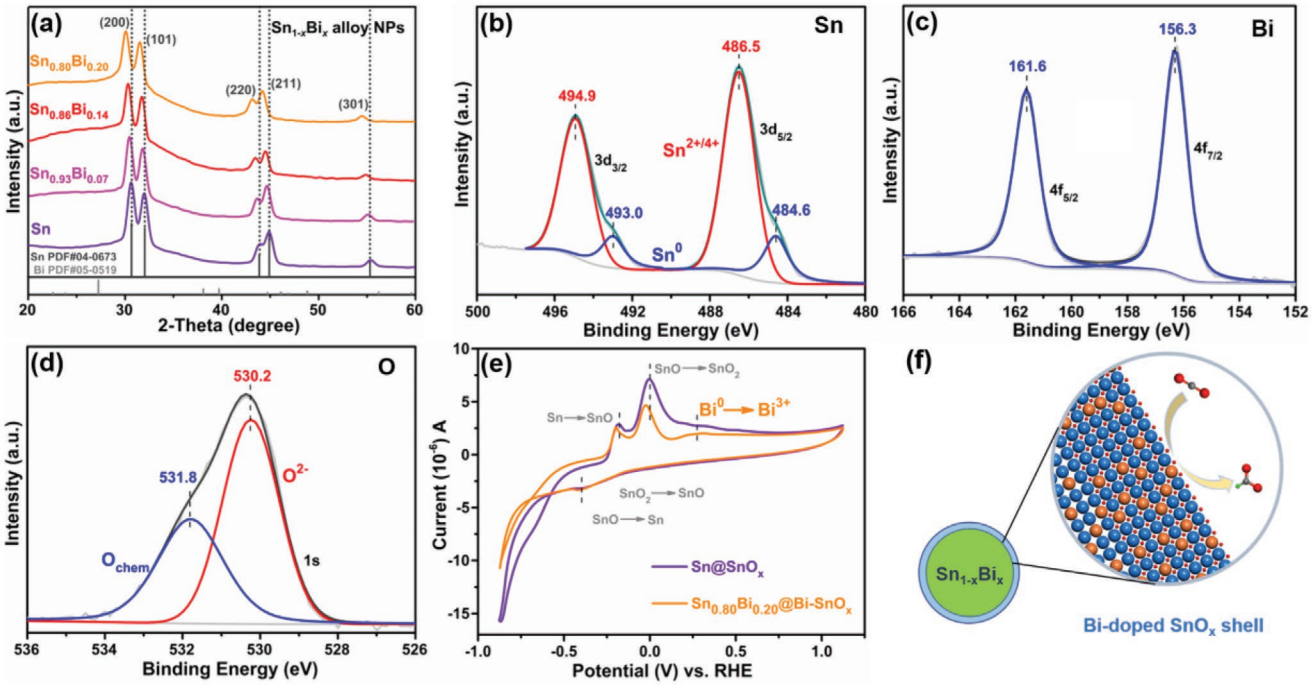

Figure 2. a) XRD patterns of $Sn_{1-x}Bi_x$ alloy NPs with different compositions. XPS spectra of $Sn_{0.80}Bi_{0.20}$ alloy NPs: b) Sn 3d, c) Bi 4f, and d) O 1s. e) CV curves of Sn and $Sn_{0.80}Bi_{0.20}$ alloy NPs. f) The structural model of Bi-doped SnO_x catalyst for CO_2 reduction.

clearly reveals the atomic structure of the $Sn_{0.80}Bi_{0.20}$ alloy NPs. The interplanar *d*-spacing of 3.36 Å in the core of the particle is slightly larger than that of (200) planes of tetrahedral Sn (2.92 Å), due to the incorporation of larger Bi atoms into the Sn crystal. An amorphous oxide nanoshell with a thickness of 3.1 nm was formed on the single-crystal core, as $Sn_{1-x}Bi_x$ alloy nanocrystals are sensitive to air exposure.[8,11] Figure 1d–g and Figures S4–S6 (Supporting Information) show EDS elemental line scan profiles and elemental mapping images of $Sn_{1-x}Bi_x$ alloy NPs, confirming the uniform distributions of Sn and Bi elements over the entire alloy NPs. The distribution of Bi element on the surface of the amorphous oxide nanoshell is also verified by atomic-resolution electron energy-loss spectroscopy (EELS) acquisitions (Figure 1h).

Phase pure $Sn_{1-x}Bi_x$ alloy NPs with tunable compositions in the range of $x = 0$–0.20 are confirmed by their XRD patterns (**Figure 2**a), which show the homogeneity of the crystal structure and absence of byproducts (such as Bi NPs). The diffraction patterns also indicate the expansion of the tetrahedral Sn lattice due to the incorporation of larger Bi atoms into Sn, which has been clearly observed via the shift of Bragg reflections to lower 2θ angles and the linear expansion of the (200) *d*-spacing with increasing Bi content (Figures S7 and S8a, Supporting Information). Simultaneously, the increase of lattice parameters in the $Sn_{1-x}Bi_x$ alloy NPs satisfies the linear relationship (Figure S8b, Supporting Information). In addition, the size distributions of the Sn and $Sn_{1-x}Bi_x$ alloy NPs obtained from Williamson-Hall[12] and Scherrer methods are very close to the statistics from TEM images (Figures S9–S10 and Table S1, Supporting Information). These consistent results further confirm the uniform size and structure of the $Sn_{1-x}Bi_x$ alloy NPs.

The structural properties of the amorphous oxide nanoshells on the $Sn_{1-x}Bi_x$ alloy NPs were further investigated by X-ray photoelectron spectroscopy (XPS) and electrochemical cyclic voltammograms (CVs). Figure 2b–d and Figure S11 (Supporting Information) show the $Sn_{0.80}Bi_{0.20}$ alloy NP survey spectrum and typical XPS fitting curves of the Sn 3d, Bi 4f, and O 1s spectra, which indicate the presence of Sn^0 (493.0 and 484.6 eV), $Sn^{4+/2+}$ (494.9 and 486.5 eV), Bi^0 (161.6 and 156.3 eV), and O^{2-} (530.2 eV) on the surface. The observed binding energy of Sn species in the $Sn_{0.80}Bi_{0.20}$ alloy NPs are slightly larger than those for the Sn NPs (Figure S12, Supporting Information), while the values for Bi are slightly smaller than the reported values.[9,13] These are due to the charge transfer between Sn and Bi or band bending across the core–shell junctions.[5a] The surface compositions obtained from XPS agree with the ICP-MS results (Table S2, Supporting Information), indicating the uniform distribution of Sn and Bi elements in the whole $Sn_{0.80}Bi_{0.20}$ core–shell NPs. CV curves of the Sn and $Sn_{0.80}Bi_{0.20}$ alloy NPs (Figure 2e) show that the surface redox potentials of the Sn species in the Sn NPs agree with a previous report,[14] while in the $Sn_{0.80}Bi_{0.20}$ alloy NPs, the two anodic peaks slightly shifted by 0.02 V to a lower potential due to the incorporation of Bi into Sn species. In addition, the reverse scan CV curve (first reduction then oxidation) of the $Sn_{0.80}Bi_{0.20}$ alloy NPs shows the absence of a reduction peak but has one broad oxidation peak of Bi^0 to Bi^{3+} (from 0.2 to 0.8 V).[7] These results indicate that the valence of Bi in the amorphous SnO_x nanoshells should be zero, which is consistent with the XPS and EELS results. The absence of Bi oxide in the nanoshells is due to the competing oxidation process of the metallic phases, according to the Bi-Sn-O phase diagram (Figure S13, Supporting Information).[8] During the competitive oxidation process, Sn atoms with higher oxygen affinity are oxidized to form amorphous SnO_x while relatively inert Bi atoms remain stable. Due to the interaction between

Sn and Bi atoms in the original β-$Sn_{1-x}Bi_x$ alloy lattice, Bi atoms are directly involved in this transformation process and are finally anchored in the as-formed amorphous SnO_x.[15] Based on the above structural characterizations, we can conclude that the $Sn_{0.80}Bi_{0.20}$ alloy NPs have a core–shell nanostructure, in which the core is crystalline $Sn_{0.80}Bi_{0.20}$ alloy and the shell is Bi-doped amorphous SnO_x, denoted as $Sn_{0.80}Bi_{0.20}$@Bi-SnO_x. In comparison, the Sn NPs possess a crystalline core of Sn and an amorphous shell of SnO_x, denoted as Sn@SnO_x. The homogeneous bimetallic alloy core of the $Sn_{0.80}Bi_{0.20}$@Bi-SnO_x NPs ensures high electrical conductivity,[6] and the tunable Bi-doped oxide nanoshell is promising for efficient CO_2 reduction (Figure 2f).

Due to the large lattice mismatch (>22%) and low solubility (<2 at%) between Sn and Bi,[16] as well as the ease of phase separation and oxidization,[8] the preparation of homogeneous $Sn_{1-x}Bi_x$ alloys to construct their oxide derivatives is challenging. The successful synthesis of novel $Sn_{1-x}Bi_x$ alloy NPs with tunable bismuth concentration (x up to 0.20) was achieved in this work. In order to further raise the composition of Bi in the $Sn_{1-x}Bi_x$ alloy NPs ($x > 0.2$), a series of attempts were performed such as the increase of BiI_3 amount and the decrease of $SnCl_2$ amount. Unfortunately, the byproducts (Bi NPs) inevitably accompanied the as-formed $Sn_{1-x}Bi_x$ alloy NPs, as shown in the XRD patterns and TEM images (Figure S14, Supporting Information). Finely tuning the reduction speed of the metal precursors ($BiCl_3$, $BiBr_3$ and BiI_3) with small redox potential differences could control the composition and size uniformity of $Sn_{1-x}Bi_x$ alloy NPs, as shown in the CV curves, XRD patterns, ICP-MS results and corresponding TEM images (Figures S15 and S16, Supporting Information). BiI_3 could be reduced more easily, as it has the most positive redox potential (0.326 V) compared with $BiCl_3$ (0.204 V) and $BiBr_3$ (0.263 V), and that help to achieve the best size uniformity in the final $Sn_{1-x}Bi_x$ alloy NPs. In addition, larger $Sn_{1-x}Bi_x$ alloy NPs can also be produced by extending the reaction time (from 10 to 30 min), as indicated by the XRD patterns and corresponding TEM images (Figures S17 and S18, Supporting Information). Meanwhile, the Bi content in these larger $Sn_{1-x}Bi_x$ alloy NPs is decreased, as indicated by the shift of Bragg reflections to higher 2θ angles and the ICP-MS results. These changes originate from the production of additional Sn species from excess $SnCl_2$ precursor during the reaction, which undergoes continuous solid diffusion within the NPs during the growth process.

The electrocatalytic CO_2 reduction properties of the Sn and $Sn_{1-x}Bi_x$ catalysts were evaluated in a gas diffusion flow cell with a three-electrode setup (Figures S19 and S22, Supporting Information). **Figure 3**a shows linear sweep voltammetry (LSV) curves of the Sn@SnO_x and $Sn_{0.80}Bi_{0.20}$@Bi-SnO_x catalysts. In Ar-saturated 0.5 M $KHCO_3$ electrolyte, the current densities measured at potentials lower than –0.68 V are attributed to the hydrogen evolution reaction (HER), which is the main competitive reaction during CO_2 reduction. In the CO_2-saturated 0.5 M $KHCO_3$ electrolyte, the dramatic increase of current densities indicates that CO_2 reduction is more favorable than the HER. The Faradaic efficiencies (FEs) of the CO_2 reduction products (CO and formate) and byproduct (H_2) were quantified by gas chromatography (GC) and nuclear magnetic resonance (NMR) spectroscopy (Figure S23, Supporting Information). For the Sn@SnO_x catalyst (Figure 3b), the FE of formate reaches a maximum value of ≈60% in the potential range from –0.98 to –1.18 V, while H_2 dominates in the low potential range from –0.68 to –0.88 V (FE of H_2: 81.5– 100%). These results indicate that the Sn@SnO_x catalyst exhibits low formate selectivity and high FE of H_2 at low potentials. In contrast, the $Sn_{0.80}Bi_{0.20}$@Bi-SnO_x catalysts possess high selectivity for formate with FEs reaching above 91.5% in a wide potential window (from –0.67 to –0.92 V). Moreover, the maximum FE reaches 95.8% at –0.88 V (Figure 3c). Thus, it's clearly indicated that products can be successfully tuned from H_2 to formate at low overpotentials. In addition, we have also investigated the catalytic performance of commercial Bi NPs, which exhibit low formate selectivity and high FE of H_2 at low overpotentials (Figure S24, Supporting Information). These results confirm that the performances of $Sn_{0.80}Bi_{0.20}$@Bi-SnO_x catalysts are superior to both of Sn@SnO_x and pure Bi NPs.

Simultaneously, the partial current density of formate on the $Sn_{0.80}Bi_{0.20}$@Bi-SnO_x catalysts is dramatically increased compared with Sn@SnO_x catalysts (Figure 3d), showing a higher current density of 20.9 mA cm^{-2} at the highest FE of 95.8% and a desirable current density of 74.6 mA cm^{-2} at a moderate potential of –1.38 V. Tauc and Nyquist plots obtained from ultraviolet visible-near infrared (UV-Vis-NIR) spectra (Figure S25, Supporting Information) and electrochemical impedance spectroscopy (Figure S26, Supporting Information) suggest that the bandgap and impedance of the $Sn_{0.80}Bi_{0.20}$@Bi-SnO_x are lower than those of Sn@SnO_x, due to the incorporation of Bi into Sn species. These results confirm that the presence of Bi in the catalysts could decrease the energy barrier and facilitate the charge-transfer process from the electrode to the adsorbed CO_2, contributing to ultrahigh current density.

To explore the effect of composition on the selectivity of CO_2 reduction, the electrocatalytic performances of two other catalysts with low Bi contents ($Sn_{0.93}Bi_{0.07}$ and $Sn_{0.86}Bi_{0.14}$ alloy NPs) have also been measured (Figures S27–S29, Supporting Information). With the increase of Bi content, the FEs of formate increase gradually from 10.9% to 95.8% at the applied potential of –0.88 V, and the HER as well as CO production are simultaneously suppressed (Figure 3e). The electrochemical active surface area (ECSA) was estimated by measuring the double-layer capacitance. As shown in Figure S30 (Supporting Information), the capacitances of these catalysts increase with the enhanced Bi contents, and the $Sn_{0.80}Bi_{0.20}$@Bi-SnO_x catalyst possesses a higher capacitance (2.79 mF cm^{-2}) than three other catalysts, including Sn@SnO_x (1.21 mF cm^{-2}), $Sn_{0.93}Bi_{0.07}$@Bi-SnO_x (1.49 mF cm^{-2}), and $Sn_{0.86}Bi_{0.14}$@Bi-SnO_x (2.35 mF cm^{-2}). As a result, theses catalysts with continuously increased ECSAs could provide more active sites for electrochemical CO_2 reduction, also contributing to its enhanced catalytic performances. Compared with current tin oxide catalysts for electrochemical CO_2 reduction, the $Sn_{0.80}Bi_{0.20}$@Bi-SnO_x catalysts exhibit the highest formate selectivity at low overpotentials (standard reduction potentials of formate: –0.02 V vs RHE),[1a] as shown in Figure 3f and Table S3 (Supporting Information). In addition, the long-term stability of the $Sn_{0.80}Bi_{0.20}$@Bi-SnO_x catalysts was also investigated, and their FEs of formate could keep a higher level (≈90%) after 50 h (Figure S31, Supporting Information). The good structure stability is revealed by a series of characterizations, including TEM, HRTEM, EDS elemental

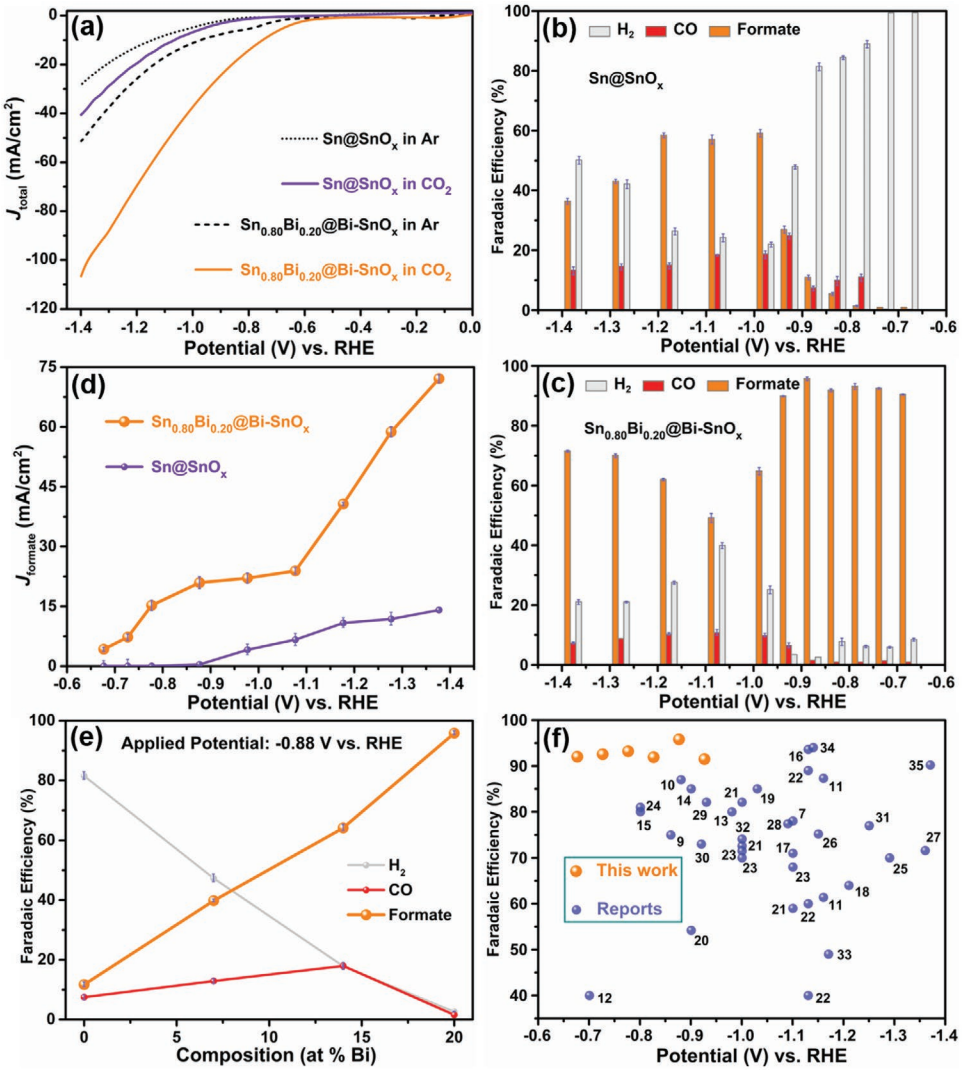

Figure 3. a) LSV of $Sn@SnO_x$ and $Sn_{0.80}Bi_{0.20}$@ Bi-SnO_x catalysts in Ar- or CO_2-saturated 0.5 M $KHCO_3$ aqueous solution (scan rate: 10 mV s^{-1}). H_2, CO, and formate FEs of b) $Sn@SnO_x$ and c) $Sn_{0.80}Bi_{0.20}$ @ Bi-SnO_x catalysts. d) Formate partial current densities of $Sn@SnO_x$ and $Sn_{0.80}Bi_{0.20}$ @ Bi-SnO_x catalysts. e) FEs for H_2, CO and formate obtained on the catalysts of Sn, $Sn_{0.93}Bi_{0.07}$, $Sn_{0.86}Bi_{0.14}$, and $Sn_{0.80}Bi_{0.20}$ at −0.88 V, respectively. f) Formate FEs of current tin oxide catalysts for electrochemical CO_2 reduction (inserted numbers represent the references in Table S3, Supporting Information).

mapping, XRD and CV (Figures S32–S34, Supporting Information). The concentration of electrolyte could affect the performances of electrocatalysts for CO_2 reduction.[4d] Therefore, $KHCO_3$ solutions with different concentrations (from 0.1 to 1 M) were used to investigate the variations of FE and production rate of formate on $Sn_{0.80}Bi_{0.20}$ @ Bi-SnO_x catalysts. As shown in Figure S35 (Supporting Information), the FE and production rate reach the highest values in 0.5 M $KHCO_3$ (95.8%, 254.9 µmol h^{-1} cm^{-2}). As the $KHCO_3$ concentration increased further, these values begin to decrease due to the enhanced hydrogen production.[4d]

To elucidate the underlying reasons for the excellent CO_2 reduction activity toward formate production on the $Sn_{0.80}Bi_{0.20}$ @ Bi-SnO_x catalyst, DFT calculations were conducted over the thermochemical energetics of CO_2 reduction and the competing HER.[17] The structural models for the DFT calculations were built based on the well-characterized Sn and $Sn_{0.80}Bi_{0.20}$ NPs, which possess a crystalline core and oxidized shell. The details are shown in Figures S36 and S37 and the Computational Section in the Supporting Information. The free energy diagrams (FEDs) for the formation of H_2, CO and HCOOH on $Sn@SnO_x$ and $Sn_{0.80}Bi_{0.20}$ @ Bi-SnO_x are presented in **Figure 4**a–c, and the magnitudes of theoretical limiting potentials $|U_L|$ are summarized in Figure 4d. It is revealed that $Sn_{0.80}Bi_{0.20}$ @ Bi-SnO_x possesses higher limiting potentials (H_2: 1.01 V, CO: 0.93 V) than those of $Sn@SnO_x$ (H_2: 0.27 V, CO: 0.65 V), indicating that $Sn_{0.80}Bi_{0.20}$ @ Bi-SnO_x has lower activities toward both H_2 and CO production. In the formation of desirable formate, the potential limiting step on the $Sn@SnO_x$ is transferring OCHO* to HCOOH, whereas it is turning CO_2 to OCHO* on the $Sn_{0.80}Bi_{0.20}$ @ Bi-SnO_x. $Sn_{0.80}Bi_{0.20}$ @ Bi-SnO_x shows an obvious lower theoretical overpotential of 0.48 V for formate formation than that of $Sn@SnO_x$ (1.09 V), suggesting that $Sn_{0.80}Bi_{0.20}$ @ Bi-SnO_x exhibits higher selectivity

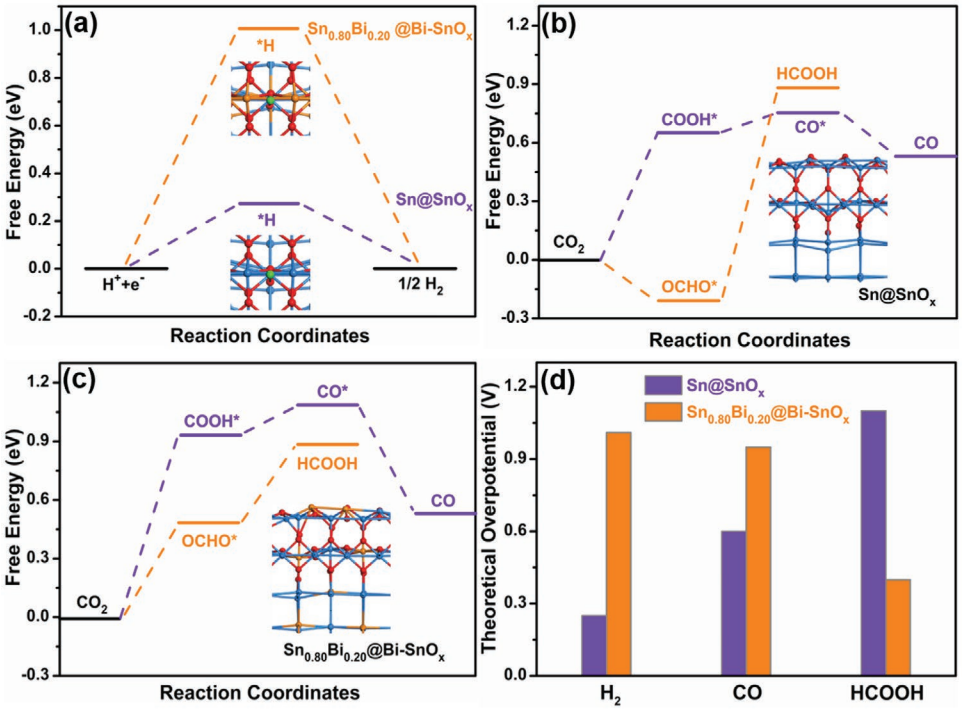

Figure 4. a–c) Free energy diagrams for H_2, CO, and HCOOH on Sn@SnO_x and $Sn_{0.80}Bi_{0.20}$@ Bi-SnO_x. d) Magnitudes of the theoretical limiting potentials of H_2, CO, and HCOOH production on stepped Sn@SnO_x and $Sn_{0.80}Bi_{0.20}$@ Bi-SnO_x.

for generating HCOOH. Hence, we conclude that the incorporation of Bi into Sn@SnO_x to form $Sn_{0.80}Bi_{0.20}$@ Bi-SnO_x not only increases the limiting potentials of H_2 and CO, but also decreases that of HCOOH, and thus significantly enhances formate selectivity. Based on these FED results, it should also be noted that the production of HCOOH on $Sn_{0.80}Bi_{0.20}$@ Bi-SnO_x is most preferential than the production of H_2 and CO at potentials from 0.48 to 0.93 V, which agrees well with the experimental results. Additionally, DFT calculations were also conducted for the pure Bi, which shows higher limiting potentials of 2.17 V for CO and 1.41 V for HCOOH compared to 1.31 V for H_2 (Figure S38, Supporting Information). These results indicate that pure Bi has the highest activity toward H_2 production, which is consistent with the experiments (Figure S24, Supporting Information). On the other hand, as revealed by the projected density of states (PDOS) at the Bi-Sn interface in a previous report,[9] the higher electronegativity of Bi could allow electrons flow easily from Sn to Bi, which would upshift the electron states of Sn away from the Fermi level, thus decreasing the energy barrier and facilitating charge-transfer from the electrode to the adsorbed CO_2.[8] These results are supported by the Tauc plots and Nyquist plots obtained from our experimental data.

In this work, novel $Sn_{1-x}Bi_x$ alloy NPs with native Bi-doped amorphous SnO_x nanoshells are synthesized for the first time. Based on combined experimental results and DFT analyses, the excellent CO_2 reduction performances of the Bi-SnO_x nanoshells derived from $Sn_{0.80}Bi_{0.20}$ alloy NPs are attributed to the incorporation of Bi into the Sn species, which could suppress hydrogen evolution and CO production and therefore facilitate formate generation. This work opens up an effective strategy for boosting catalytic reactions by creating atom-doped amorphous oxide surfaces derived from novel bimetallic alloys.

Experimental Section

Experimental details are provided in the Supporting Information.

Supporting Information

Supporting Information is available from the Wiley Online Library or from the author.

Acknowledgements

Q.Y., Q.W., and Y.L. contributed equally to this work. This work was supported by the National Natural Science Foundation of China (NSFC) (Grant 51772142), the Science and Technology Cooperation Fund between Chinese and Australian Governments (Grant 2017YFE0132300), the Guangdong Science and Technology Department (Grant 2016ZT06C279), the Shenzhen Science and Technology Innovation Committee (Grants JCYJ20170412152528921 and KQTD2016053019134356), the Guangxi Science and Technology Project (AA17204083 and AB16380030), the link project of the National Natural Science Foundation of China and Fujian Province (U1705252), and the SUSTech Presidential Fund.

Conflict of Interest

The authors declare no conflict of interest.

Keywords

CO_2 electroreduction, core–shell nanostructures, formate, novel $Sn_{1-x}Bi_x$ alloys

Received: April 26, 2020
Revised: June 11, 2020
Published online:

[1] a) C. Xie, Z. Niu, D. Kim, M. Li, P. Yang, *Chem. Rev.* **2020**, *120*, 1184; b) Y. Wu, Z. Jiang, X. Lu, Y. Liang, H. Wang, *Nature* **2019**, *575*, 639; c) Z. Liang, W. Guo, R. Zhao, T. Qiu, H. Tabassum, R. Zou, *Nano Energy* **2019**, *64*, 103917; d) C. Dai, L. Sun, J. Song, H. Liao, A. C. Fisher, Z. J. Xu, *Small Methods* **2019**, *3*, 1900362; e) H. Tabassum, A. Mahmood, B. Zhu, Z. Liang, R. Zhong, S. Guo, R. Zou, *Energy Environ. Sci.* **2019**, *12*, 2924; f) Z. Quan, Z. Luo, W. S. Loc, J. Zhang, Y. Wang, K. Yang, N. Porter, J. Lin, H. Wang, J. Fang, *J. Am. Chem. Soc.* **2011**, *133*, 17590; g) J. Song, C. Wei, Z. F. Huang, C. Liu, L. Zeng, X. Wang, Z. J. Xu, *Chem. Soc. Rev.* **2020**, *49*, 2196; h) Q. Wei, S. Wu, Y. Sun, *Adv. Mater.* **2018**, *30*, 1802082; i) M. G. Kibria, J. P. Edwards, C. M. Gabardo, C.-T. Dinh, A. Seifitokaldani, D. Sinton, E. H. Sargent, *Adv. Mater.* **2019**, *31*, 1807166; j) J. Wu, Y. Huang, W. Ye, Y. Li, *Adv. Sci.* **2017**, *4*, 1700194.

[2] a) S. Zhu, Q. Wang, X. Qin, M. Gu, R. Tao, B. P. Lee, L. Zhang, Y. Yao, T. Li, M. Shao, *Adv. Energy Mater.* **2018**, *8*, 1802238; b) J. Huang, M. Mensi, E. Oveisi, V. Mantella, R. Buonsanti, *J. Am. Chem. Soc.* **2019**, *141*, 2490.

[3] a) C. H. Lee, M. W. Kanan, *ACS Catal.* **2015**, *5*, 465; b) Z. Zhang, F. Ahmad, W. Zhao, W. Yan, W. Zhang, H. Huang, C. Ma, J. Zeng, *Nano Lett.* **2019**, *19*, 4029.

[4] a) Y. Wei, J. Liu, F. Cheng, J. Chen, *J. Mater. Chem. A* **2019**, *7*, 19651; b) S. Liu, J. Xiao, X. F. Lu, J. Wang, X. Wang, X. W. Lou, *Angew. Chem., Int. Ed.* **2019**, *58*, 8499; c) Q. Zhang, Y. Zhang, J. Mao, J. Liu, Y. Zhou, D. Guay, J. Qiao, *ChemSusChem* **2019**, *12*, 1443; d) L. Peng, Y. Wang, I. Masood, B. Zhou, Y. Wang, J. Lin, J. Qiao, F. Zhang, *Appl. Catal., B* **2020**, *264*, 118447; e) X. Hou, Y. Cai, D. Zhang, L. Li, X. Zhang, Z. Zhu, L. Peng, Y. Liu, J. Qiao, *J. Mater. Chem. A* **2019**, *7*, 3197.

[5] a) Q. Li, J. Fu, W. Zhu, Z. Chen, B. Shen, L. Wu, Z. Xi, T. Wang, G. Lu, J. J. Zhu, S. Sun, *J. Am. Chem. Soc.* **2017**, *139*, 4290; b) N. S. Porter, H. Wu, Z. Quan, J. Fang, *Acc. Chem. Res.* **2013**, *46*, 1867; c) A. Zhang, R. He, H. Li, Y. Chen, T. Kong, K. Li, H. Ju, J. Zhu, W. Zhu, J. Zeng, *Angew. Chem., Int. Ed.* **2018**, *57*, 10954; d) Z. Geng, X. Kong, W. Chen, H. Su, Y. Liu, F. Cai, G. Wang, J. Zeng, *Angew. Chem., Int. Ed.* **2018**, *57*, 6054; e) X. Wang, Q. Zhao, B. Yang, Z. Li, Z. Bo, K. H. Lam, N. M. Adli, L. Lei, Z. Wen, G. Wu, Y. Hou, *J. Mater. Chem. A* **2019**, *7*, 25191; f) F. Pan, H. Zhang, Z. Liu, D. Cullen, K. Liu, K. More, G. Wu, G. Wang, Y. Li, *J. Mater. Chem. A* **2019**, *7*, 26231; g) X. Li, X. Li, C. Liu, H. Huang, P. Gao, F. Ahmad, L. Luo, Y. Ye, Z. Geng, G. Wang, R. Si, C. Ma, J. Yang, J. Zeng, *Nano Lett.* **2020**, *20*, 1403; h) S. Luo, W. Chen, Y. Cheng, X. Song, Q. Wu, L. Li, X. Wu, T. Wu, M. Li, Q. Yang, K. Deng, Z. Quan, *Adv. Mater.* **2019**, *31*, 1903683; i) P. Wang, M. Qiao, Q. Shao, Y. Pi, X. Zhu, Y. Li, X. Huang, *Nat. Commun.* **2018**, *9*, 4933.

[6] W. Luc, C. Collins, S. Wang, H. Xin, K. He, Y. Kang, F. Jiao, *J. Am. Chem. Soc.* **2017**, *139*, 1885.

[7] a) H. Yang, N. Han, J. Deng, J. Wu, Y. Wang, Y. Hu, P. Ding, Y. Li, Y. Li, J. Lu, *Adv. Energy Mater.* **2018**, *8*, 1801536; b) N. Han, Y. Wang, H. Yang, J. Deng, J. Wu, Y. Li, Y. Li, *Nat. Commun.* **2018**, *9*, 1320; c) X. Zhang, J. Fu, Y. Liu, X. Zhou, J. Qiao, *ACS Sustainable Chem. Eng.* **2020**, *8*, 4871; d) X. Zhang, X. Hou, Q. Zhang, Y. Cai, Y. Liu, J. Qiao, *J. Catal.* **2018**, *365*, 63.

[8] J. Tang, R. Daiyan, M. B. Ghasemian, S. A. Idrus-Saidi, A. Zavabeti, T. Daeneke, J. Yang, P. Koshy, S. Cheong, R. D. Tilley, R. B. Kaner, R. Amal, K. Kalantar-Zadeh, *Nat. Commun.* **2019**, *10*, 4645.

[9] G. Wen, D. U. Lee, B. Ren, F. M. Hassan, G. Jiang, Z. P. Cano, J. Gostick, E. Croiset, Z. Bai, L. Yang, Z. Chen, *Adv. Energy Mater.* **2018**, *8*, 1802427.

[10] T. Yuan, Z. Hu, Y. Zhao, J. Fang, J. Lv, Q. Zhang, Z. Zhuang, L. Gu, S. Hu, *Nano Lett.* **2020**, *20*, 2916.

[11] a) X. Zhao, Q. Di, X. Wu, Y. Liu, Y. Yu, G. Wei, J. Zhang, Z. Quan, *Chem. Commun.* **2017**, *53*, 11001; b) Q. Yang, X. Zhao, X. Wu, M. Li, Q. Di, X. Fan, J. Zhu, X. Song, Q. Li, Z. Quan, *Chem. Mater.* **2019**, *31*, 2248; c) X. Zhao, Q. Di, M. Li, Q. Yang, Z. Zhang, X. Guo, X. Fan, K. Deng, W. Chen, J. Zhang, J. Fang, Z. Quan, *Chem. Mater.* **2019**, *31*, 4325; d) X. Zhao, Q. Yang, Z. Quan, *Chem. Commun.* **2019**, *55*, 8683; e) Y. Sun, X. Zuo, S. K. R. S. Sankaranarayanan, S. Peng, B. Narayanan, G. Kamath, *Science* **2017**, *356*, 303.

[12] A. Khorsand Zak, W. H. Abd Majid, M. E. Abrishami, R. Yousefi, *Solid State Sci.* **2011**, *13*, 251.

[13] Z. Zhang, M. Chi, G. M. Veith, P. Zhang, D. A. Lutterman, J. Rosenthal, S. H. Overbury, S. Dai, H. Zhu, *ACS Catal.* **2016**, *6*, 6255.

[14] W. Ju, J. Zeng, K. Bejtka, H. Ma, D. Rentsch, M. Castellino, A. Sacco, C. F. Pirri, C. Battaglia, *ACS Appl. Energy Mater.* **2019**, *2*, 867.

[15] E. A. Sutter, X. Tong, K. Jungjohann, P. W. Sutter, *Proc. Natl. Acad. Sci. USA* **2013**, *110*, 10519.

[16] H. Okamoto, *J. Phase Equilib. Diffus.* **2010**, *31*, 205.

[17] a) K. Mathew, R. Sundararaman, K. Letchworth-Weaver, T. A. Arias, R. G. Hennig, *J. Chem. Phys.* **2014**, *140*, 084106; b) J. P. Perdew, K. Burke, M. Ernzerhof, *Phys. Rev. Lett.* **1996**, *77*, 3865; c) X. Zheng, Y. Ji, J. Tang, J. Wang, B. Liu, H.-G. Steinrück, K. Lim, Y. Li, M. F. Toney, K. Chan, Y. Cui, *Nat. Catal.* **2019**, *2*, 55.